Molecular Therapy
Nucleic Acids
Original Article

L-Type amino acid transporter 1-targeting nanoparticles for antisense oligonucleotide delivery to the CNS

Yu Na Lim,[1,5] In Soo Ryu,[1,5] Yeon-Joo Jung,[1] Gabriel Helmlinger,[1] Insun Kim,[1] Hye Won Park,[1] Hansol Kang,[1] Jina Lee,[1] Hyo Jin Lee,[1] Kang Seon Lee,[1] Ha-Na Jang,[1] Dae-In Ha,[1] Junghyung Park,[2] Jinyoung Won,[2] Kyung Seob Lim,[3] Chang-Yeop Jeon,[2] Hyun-Jeong Cho,[4] Hyun Su Min,[1] and Jin-Hyeob Ryu[1]

[1]BIORCHESTRA Co., Ltd, 1, Gukjegwahak 2-ro, Yuseong-gu, Daejeon 34000, South Korea; [2]National Primate Research Center, Korea Research Institute of Bioscience and Biotechnology (KRIBB), Cheongju 28116, South Korea; [3]Futuristic Animal Resource and Research Center, Korea Research Institute of Bioscience and Biotechnology (KRIBB), Cheongju 28116, South Korea; [4]Department of Biomedical Laboratory Science, College of Medical Science, Konyang University, Daejeon 35365, South Korea

L-Type amino acid transporter 1 (LAT1)-specific ligands and polyion complexes are used as brain-specific targets to deliver RNA-based drugs across the blood-brain barrier. We characterized an LAT1-targeting antisense oligonucleotide (ASO)-encapsulated nanoparticle, Phe-NPs/ASO. A 25% density of phenylalanine effectively binds to the surface of LAT1-targeting NPs in the GL261-Luc cells, and Phe-NPs/ASO shows higher binding affinity compared to that without phenylalanine by cellular binding assay. To further characterize the blood-brain barrier-targeting effect and tissue distribution following a single-dose intravenous injection in mice, we performed *in vivo* biodistribution studies using fluorescence imaging. The Phe-NPs/ASOs were detected in the brain tissue 1 h post-intravenous injection at an approximately 64-fold higher ratio than that of the same ASOs administered in the absence of any NP carrier. The brain tissue delivery of ASO-loaded Phe-NPs was also confirmed in a fluorescence imaging study performed in non-human primates. These results demonstrate that Phe-NPs may successfully deliver an ASO to the brain tissue across brain regions. Phe-NPs loaded with RNA-based drugs have the potential to treat diseases of the CNS, including all forms of neurodegenerative diseases.

INTRODUCTION

RNA-based drugs have great potential for treating diseases by modulating gene expression through various RNA-mediated processes, such as RNAi and target gene degradation. As therapeutic agents, oligonucleotides have recently become of substantial interest; however, the select, effective, and safe delivery of oligonucleotide-based drugs to target tissues remains a challenge for broader therapeutic applications. Progress has been made regarding various RNA modification-chemistry technologies aimed at enhancing RNA stability and pharmacological effects via sequence modification and the addition of various moieties. Modified antisense oligonucleotides (ASOs), which are currently approved as drugs or in clinical development, have been designed to target genetic mutations. Most of these ASOs are administered intrathecally (IT) or intracerebroventricularly (ICV).[1–5] However, these advanced chemical modifications of oligonucleotide drugs do not fully resolve the challenge of selective, targeted delivery to diseased organs and tissues of interest while minimizing delivery to non-diseased tissues, thereby managing safety more effectively. Novel drug delivery systems are required, particularly when attempting to treat devastating diseases in hard-to-reach organs featuring blood-tissue barriers, such as the CNS, and under drug administration conditions that are less invasive than IT or ICV. Thus, we sought to develop a specific, brain-targeting, nanoparticles (NPs)-based delivery system for RNA-based drug cargoes that would achieve pharmacologically relevant drug concentrations in the CNS while controlling excessive drug exposure in non-diseased, non-target organs.

Recently, specific receptor- and transporter-mediated NPs have been developed to deliver RNA-based drugs across the blood-brain barrier (BBB) and CNS into specific brain cell types.[6–8] Transferrin, low-density lipoprotein, nicotinic acetylcholine, insulin, and insulin-like growth factor receptors have been studied for drug delivery through receptor-mediated transcytosis.[9,10] In addition, a transport vehicle targeting CD98hc enabled prolonged brain exposure, compatibility, and distinctive kinetics.[11] A choline-modified doxorubicin-polyethylene glycol (PEG) polymer conjugate was developed for brain targeting and glioma therapy.[12] L-Carnitine conjugated to poly (lactic-co-glycolic acid)-modified NPs was prepared for glioma cell targeting.[13,14] Our brain drug delivery design strategy revolved around targeting NP carriers with drug cargo to transporters and receptors overexpressed in the endothelium, which is an integral part of

Received 4 April 2024; accepted 12 September 2024;
https://doi.org/10.1016/j.omtn.2024.102340.

[5]These authors contributed equally

Correspondence: Hyun Su Min, BIORCHESTRA Co., Ltd., 1, Gukjegwahak 2-ro, Yuseong-gu, Daejeon, 34000, South Korea
E-mail: min@biorchestra.com
Correspondence: Jin-Hyeob Ryu, BIORCHESTRA Co., Ltd., 1, Gukjegwahak 2-ro, Yuseong-gu, Daejeon, 34000, South Korea
E-mail: branden.ryu@biorchestra.com

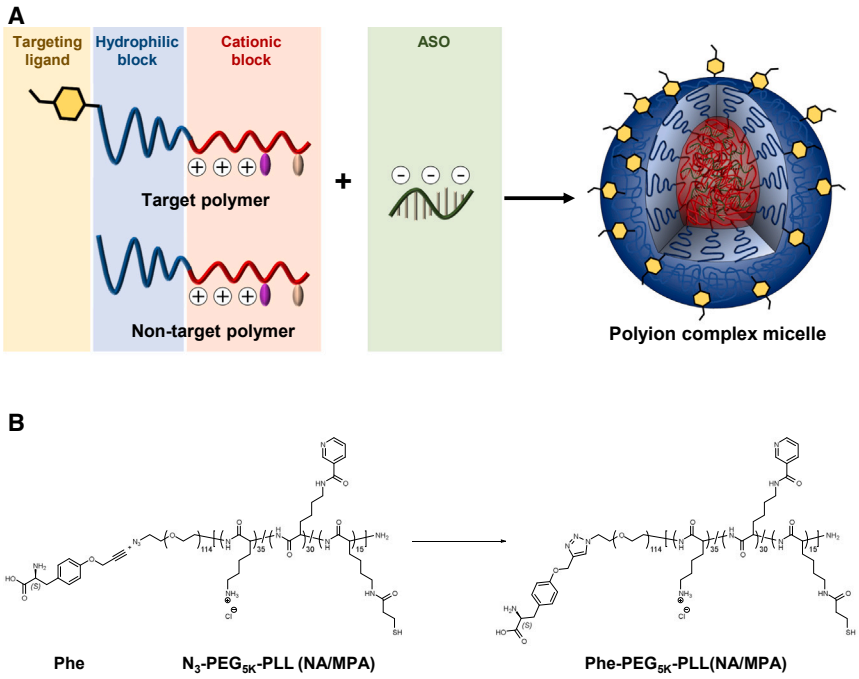

Figure 1. Schematic illustration of ASO-loaded Phe-PEG-PLL(NA/MPA)

(A) PEG-PLL(NA/MPA) with and without Phe ligand complex with ASO drug cargo. Cationic block and hydrophilic block of polymer chains allow for rapid dissociation and intracellular release of the ASO cargo. (B) Phe-PEG-PLL(NA/MPA) synthesis schematic. Phe was introduced through a click reaction between N_3-PEG-PLL(NA/MPA) and the alkyne modified tyrosine.

the BBB. These NPs would then cross the BBB to reach the CNS via transporter-, receptor-, or adsorption-mediated transcytosis and endocytosis.[15–22] However, the brain delivery efficiency of currently designed nanomaterials with nucleic acid cargoes is relatively low and insufficient in drug cargo concentrations to induce pharmacologically driven therapeutic effects within the CNS.[23–26] To achieve specificity in molecular material transport across the BBB, most studies have focused on the conjugation of targeting moieties, such as ligands, antibodies, aptamers, transferrin, and glycosidic moieties, to the surface of lipid-based or polymeric NPs.[27,28]

The L-type amino acid transporter 1 (LAT1), also known as *SLC7A5*, is one of the most extensively investigated transporters for drug delivery across the BBB. This amino acid transporter is involved in cell proliferation and differentiation through the uptake of essential amino acids.[29–31] LAT1 in the BBB has a high binding affinity for amino acids, such as isoleucine, phenylalanine (Phe), methionine, tyrosine, histidine, and tryptophan.[32–34] It forms a heterodimer[35–37] with CD98hc and is expressed on the plasma membrane of brain capillary endothelial cells (BCECs) in the BBB. LAT1 plays an important role in the delivery of amino acids and hormones and in the delivery of clinically used drugs such as gabapentin, pregabalin, levodopa, and melphalan so that these molecules reach their target sites in the brain.[35–37] Studies have further shown that LAT1 is highly expressed not only in endothelial cells of the BBB but also in brain cells such as neurons, astrocytes, and glial cells, making this transporter attractive for BBB crossing and for brain cell uptake of a particular drug once it has reached the CNS.[33,38,39] In glioblastomas, LAT1-targeted NPs encapsulating the drugs temozolomide and sorafenib induce synergistic anticancer effects following the buildup of these drugs to pharmacologically active levels in brain tissue, once they have moved beyond the BBB.[40,41] However, LAT1-targeting NPs with an RNA-based drug cargo have not been investigated.

Thus, we sought to develop an LAT1-targeting NP for the delivery of an ASO cargo to the CNS, with the following design strategy to optimize tissue delivery: (1) a size of NPs in the range of 15–50 nm to maximize BBB endo- or transcytosis; (2) a sufficient half-life of NPs in blood circulation following systemic intravenous (IV) administration, and (3) an optimal density of LAT1 ligands at the surface of polymer-based NPs to maximize binding to BCECs and crossing of the BBB over time.[33,34,40,42] Based on this design strategy, we developed BIORCHESTRA's Drug Delivery System to generate an NP carrier encapsulating an RNA-based drug cargo of choice, an ASO. The building blocks consisted of PEG and poly-L-lysine (PLL) copolymer chains (later amended with LAT1 ligands), which, upon polyion complexation with ASO molecules in solution, self-assembled into NPs, effectively encapsulating the ASO molecules. In the present study, we addressed that brain-targeting NPs with ASO cargo systemically deliver the ASOs to the brain.

RESULTS

Preparation and characterization of the NPs: Polymer constituents and ASO-loaded micelle formation

LAT1-targeting ASO-loaded NPs were formed by exploiting the ionic interactions between ASO molecules and poly(ethylene glycol)-*b*-poly(L-lysine) (PEG-PLL) cationic polymer chains. The LAT1-targeting ligand density on the external surface of the NPs was controlled by optimizing the ratio of targeting (with Phe) to non-targeting (without Phe) polymer quantities in solution (Figure 1A).

To obtain polyion-complexed micelles with a stable structure, a hydrophobic component and a cross-linkable adjunct moiety were considered in the design of the polymers. Nicotinamide (NA) and 3-mercaptopropanamide (MPA) were introduced to enhance micellar stability through hydrophobic interactions and cross-linking at the core upon NP formation. NA and MPA also helped control drug cargo release kinetics from the NPs, since the pKa of the pyridine ring in NA is 5.8 and the disulfide bonds formed by MPA after NP formation may be cleaved under low pH or high glutathione (GSH) conditions. In the synthesis of LAT1-targeting and non-targeting

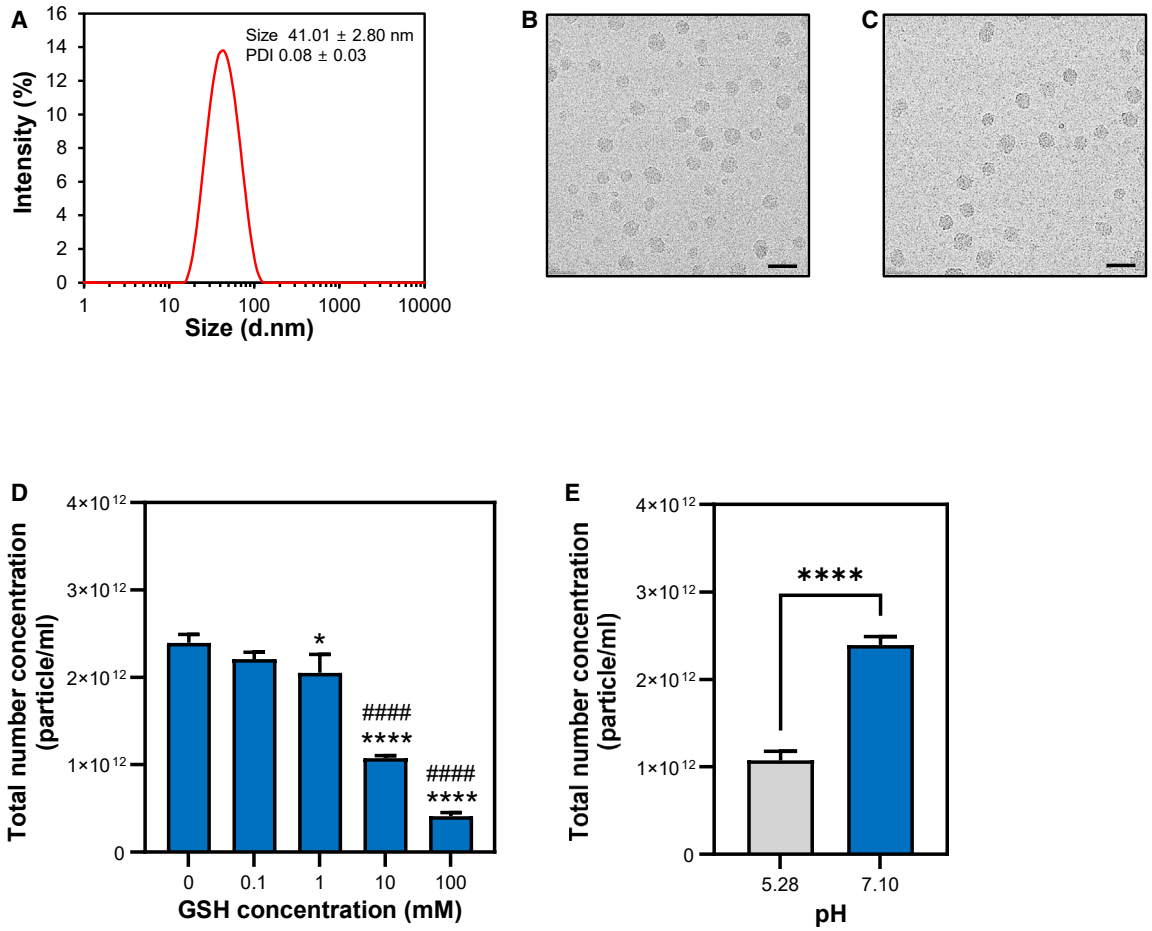

Figure 2. Characterization studies of Phe-NPs/ASO

(A) Hydrodynamic size distribution of Phe-NPs/ASO. (B) Morphologies of Phe-NPs/ASO observed by a cryo-transmission electron microscope before lyophilization and (C) after lyophilization. Scale bar: 50 nm. (D) Changes in total ASO concentration in synthesized Phe-NPs/ASO under various GSH concentrations (0, 0.1, 1.0, 10, and 100 mM). Data are presented as means ± SDs (one-way ANOVA and Tukey multiple comparisons tests; $^{*}p < 0.05$, $^{****}p < 0.0001$ vs. 0 mM GSH, $^{\#\#\#\#}p < 0.001$ vs. 1 mM GSH). (E) Total ASO concentration in synthesized Phe-NPs/ASO under varying pH conditions (pH 5.28 and pH 7.10). Data are presented as means ± SDs (unpaired t test, $^{****}p < 0.001$ vs. pH 5.28).

polymers, equal amounts of NA and 3,3′-dithiodipropionic acid (DTDPA) were added to azido-poly(ethylene glycol)-*b*-poly(L-lysine) (N_3-PEG-PLL(NH_2)) or monomethoxy-poly(ethylene glycol)-*b*-poly(L-lysine) (MeO-PEG-PLL(NH_2)) polymers to form NA and MPA on the side chains of the lysine groups through *N*-(3-dimethylaminopropyl)-*N*′-ethylcarbodiimide hydrochloride/*N*-hydroxysuccinimide (EDC/NHS) coupling reactions. Pale yellow powders of N_3-PEG-PLL(NA/MPA) and MeO-PEG-PLL(NA/MPA) were obtained in 90% and 85% yields, respectively. The chemical structures and compositions of both polymers were characterized by ^{1}H-NMR (Figures S1–S3). An additional reaction was conducted to synthesize the LAT1-targeting polymer. H-L-Tyr(propargyl)-OH, which features an alkyne structure at the end of the Phe ligands (Figures S4 and S5), was conjugated to N_3-PEG-PLL(NA/MPA) via a click reaction to form Phe-PEG-PLL(NA/MPA) with a triazole linkage (Figure 1B). The conjugation ratio of the Phe ligands to the targeting polymer was greater than 99%, as calculated based on ^{1}H-NMR measurements (Figure S6). To further characterize NPs, we performed dynamic light scattering analyses. Phe-NPs/ASO exhibited a size of approximately 41.01 ± 2.80 nm and a polydispersity index (PDI) of 0.08 ± 0.03 (Figure 2A). As shown in Figures 2B and 2C, the overall morphology of Phe-NPs/ASO before and after lyophilization was assessed using cryo-transmission electron microscopy (cryo-TEM) imaging. Their physical size was <50 nm, demonstrating highly homogeneous NP sizes during preparation. Detailed characteristics in size distribution, zeta potential, pH, and encapsulation efficiency (EE%) of NPs before and after lyophilization are shown in Table 1. These data indicated that the morphology of the NPs remained unchanged before and after lyophilization. Additionally, the results showed that particle numbers of NPs progressively decreased and therefore dissociated in the presence of 1.0, 10, or 100 mM GSH ($F_{(4,13)} = 169.9$, $p < 0.0001$; Figure 2D). Moreover, Phe-NPs/ASO

Table 1. Characterization of Phe-NPs/ASO before and after lyophilization

Phe-NPs/ASO	Size, diameter, nm	PDI	Zeta potential, mV	pH	EE%
Before lyophilization	41.01 ± 2.80	0.08 ± 0.03	26.3 ± 3.15	7.36 ± 0.07	94.8 ± 0.81
After lyophilization	42.40 ± 0.41	0.07 ± 0.004	26.5 ± 0.31	7.29 ± 0.05	–

exhibited a pH-dependent dissociation behavior ($t_{(7)}$ = 18.30, p < 0.0001; Figure 2E). At pH 5.28, particle numbers decreased compared to particles at pH 7.10, indicative of NP dissociation. The GSH and pH parameters controlling NP dissociation kinetics were dependent on the MPA or NA characteristics.

In vitro characterization of Phe-NPs/ASO: Cellular uptake, endosomal escape, cell viability, and cytotoxicity

Cellular internalization of NPs was dependent on the LAT1 ligand density on the outer surface of the NPs.[43] To determine the optimal density of LAT1 ligands, we quantified cellular uptake of NPs containing naked Cy5.5-labeled ASO cargo molecules (ASO-Cy5.5) with varying percentages of Phe ligands (0%, 25%, 50%, 75%, and 100%) in LAT1-expressing GL261-Luc cells using flow cytometry. The NPs (containing 300 nM ASOs) with varying ligand density, which have a size of 42–45 nm (PDI <0.2), were added to cells and incubated for 30 min. The percentages of Cy5.5$^+$ GL-261-Luc cells after NP exposure was significantly increased compared to that observed in cells treated with ASO-Cy5.5 ($F_{(6,14)}$ = 272.1, p < 0.0001), while the percentage of Cy5.5$^+$ cells also varied depending on the Phe ligand densities at the surface of NPs (Figure 3A). In particular, treatment with NPs featuring a 25%-Phe ligand density showed an approximately 2-fold increase in intensity, as compared to NPs with 0%-Phe ligand density (p < 0.001). At 25%-Phe, NPs also exhibited higher fluorescence intensities as compared to the 75%-Phe and 100%-Phe ligand density groups, while intensities in that 25%-Phe group were comparable to those measured in the 50%-Phe group (p < 0.001 vs. 75%-Phe group; p < 0.01 vs. 100%-Phe group; p = 0.43 vs. 50%-Phe group) (Figure 3A). We considered a 25%-Phe ligand density on the surface of LAT1-targeting NPs to be adequate.

We further evaluated NP targetability using a cellular binding assay and by testing Cy5.5-labeled ASO-loaded NPs with 0%-Phe ligand density (NT-NPs/ASO-Cy5.5) and NPs with 25%-Phe ligand density (Phe-NPs/ASO-Cy5.5), with or without Phe ligand molecules, against highly expressing LAT1 GL261-Luc cells. The size of each NPs was around 40 nm and had 26 mV of surface charge (Table S1). In the absence of Phe ligand molecules, exposure to Phe-NPs/ASO-Cy5.5 resulted in an approximately 3-fold higher fluorescence intensity compared to exposure to NT-NPs/ASO-Cy5.5 ($t_{(6)}$ = 4.465, p < 0.01) (Figure 3B). In the presence of Phe ligands, the fluorescence intensities of Phe-NPs/ASO-Cy5.5-exposed cells were considerably lower than those of NT-NPs/ASO-Cy5.5-treated cells ($t_{(6)}$ = 0.2946, p = 0.7782) (Figure 3B).

Endosomal escape is essential for the efficient cytosolic delivery of nanocarrier drug cargoes to act biologically.[44,45] Therefore, we tested *in vitro* the time-dependent endosomal escape of ASO molecules from our NPs. GL261-Luc cells were exposed to Phe-NPs/ASO-Cy5.5, incubated for 1 h, and washed with fresh cell culture medium. The cells were then incubated for 0, 1, 2, or 4 h. Our image analyses showed that Cy5.5 fluorescence was detected in the cytoplasm at the 0 h time point and co-localized with the green fluorescence signal corresponding to endosomal structures. After 1–2 h of incubation, the intensities of both the green and red fluorescence signals increased and co-localized puncta were detected. After a 4 h incubation period, co-localized puncta decreased in number compared to that with shorter incubation times, while the red puncta fluorescence signal increased (Figures 3C and 3D). These data demonstrate, mechanistically, that Phe-NPs/ASO-Cy5.5, once taken up intracellularly, may release ASO cargo via an effective endosomal escape process. Our data showed that kinetically, this escape process may be active approximately 1–4 h following cellular internalization of the NPs. To exclude any potential effects of these NPs on cellular toxicity, we investigated the viability and cytotoxicity of NT-NPs/ASO and Phe-NPs/ASO in GL261-Luc cells. The GL261-Luc cells were exposed to various concentrations of NT-NPs/ASO or Phe-NPs/ASO for 48 h. There were no significant effects on cell viability or cytotoxicity following exposure to NT-NPs/ASO or Phe-NPs/ASO at any of the tested concentrations (Figures S7A and S7B).

LAT1 gene and protein expression in brain cells and tissues

To assess the expression of the LAT1 (*SLC7A5*) gene in the brains of humans and non-human species (including *Macaca fascicularis*, *Rattus norvegicus*, and *Mus musculus*), we conducted an exhaustive analysis of published RNA sequencing data (Figure S8). *SLC7A5* was expressed at a level similar to or higher than the average expression of all other genes in the brains of humans and non-humans (Figure S8). We also investigated *SLC7A5* expression in the brains of healthy humans and patients with Alzheimer disease (AD). There were no significant differences in *SLC7A5* expression between the two groups (p = 0.9660) (Figure S8). Consistently, we found that the LAT1 protein was highly expressed in cultured neuronal and glial cells (Figure S9). The level of LAT1 expression in the brain differed slightly among brain regions; it was generally co-expressed with the CD31 protein, a marker of BCECs, throughout the brains of mice and monkeys (Figure S10). Therefore, LAT1 is abundantly expressed in BCECs of the BBB.

Pharmacokinetics and biodistribution of Phe-NPs/ASO in the mouse

To evaluate the targeting effect and time-dependent biodistribution of Phe-NPs/ASO, we conducted an *in vivo* fluorescence imaging biodistribution study in mice following the IV administration of the

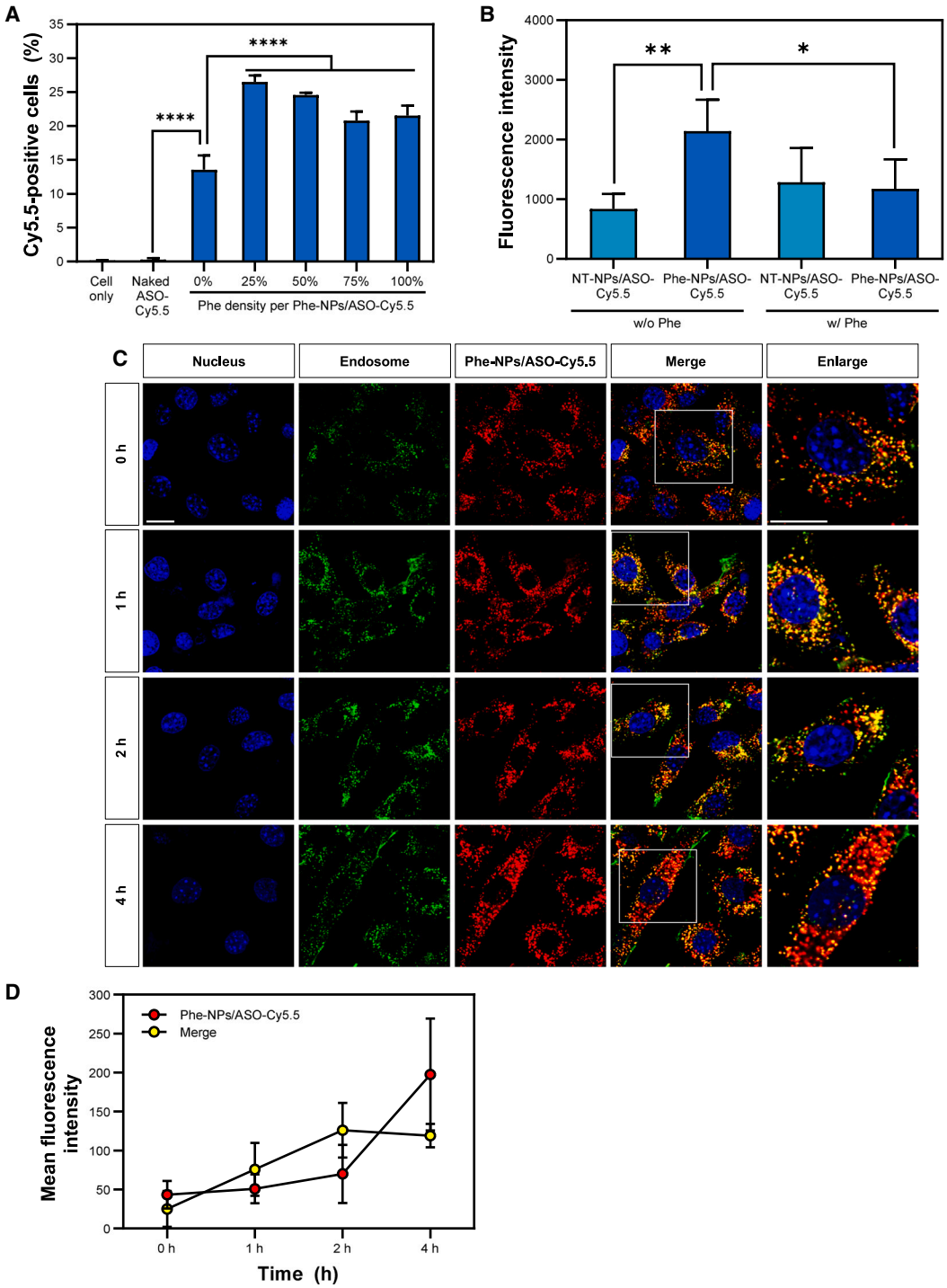

Figure 3. *In vitro* characterization of Phe-NPs/ASO-Cy5.5

(A) Quantification of Phe-NPs/ASO-Cy5.5 cellular uptake in a GL261-Luc cell line, at varying Phe ligand densities. (B) Changes in Cy5.5 fluorescence intensities following exposure to targeting Phe-NPs/ASO-Cy5.5 or NT-NP$_S$/ASO-Cy5.5 in the absence or presence of a Phe inhibitor; GL261-Luc cell line. Data are presented as means ± SDs (one-way ANOVA and Tukey multiple comparison tests; $^*p < 0.05$; $^{**}p < 0.01$; $^{****}p < 0.0001$). (C) Confocal microscopy imaging of Phe-NPs/ASO-Cy5.5 cellular uptake in GL261-Luc cells; 0, 1, 2, and 4 h of incubation with Phe-NPs/ASO-Cy5.5. Cell nuclei were stained with DAPI (blue), acidic organelles were labeled using LysoTracker (green), and ASO-Cy5.5 was detected under red fluorescence. Scale bars: 20 μm. (D) Temporal changes in mean fluorescence intensity of Phe-NPs/ASO-Cy5.5 alone and its co-localization with acidic organelles.

particles. As shown in Figure 4, we injected the ASO-Cy5.5, or the LAT1-targeting Phe-NPs/ASO-Cy5.5 particles, or the LAT1-non-targeting NT-NPs/ASO-Cy5.5 particles at a total ASO concentration of 1 mg/kg in each case through the tail veins of mice. We subsequently monitored systemic fluorescence imaging for up to 24 h. In the ASO-Cy5.5 group, the fluorescence signal was mostly distributed in the kidney from 5 min post-IV injection and for up to 60 min and was then rapidly eliminated (Figure 4A). In the Phe-NPs/ASO-Cy5.5-treated group, an intense fluorescence signal was detected at the whole-body level, including the head area, with maximal intensity approximately 10 min post-IV injection. A moderate fluorescence signal was detected in the head area for up to 480 min (8 h) post-IV injection. In contrast, the NT-NPs/ASO-Cy5.5-treated group showed only a moderate fluorescence signal in the whole organism, as compared to the Phe-NPs/ASO-Cy5.5-treated group, at 5, 10, and 60 min time points. Additionally, the fluorescence signal in the head area was lower than the signal detected in the Phe-NPs/ASO-Cy5.5-treated group at all time points. These results indicate that in mice, Phe-NPs/ASO-Cy5.5 favorably localized in the brain region compared to the naked ASO or NT-NPs/ASO-Cy5.5 groups.

We also measured the fluorescence intensity signals in the blood of mice administered 1 mg/kg IV of either ASO-Cy5.5 or Phe-NPs/ASO-Cy5.5 as an indicator of ASO pharmacokinetics. The Phe-NPs/ASO-Cy5.5 fluorescence signal half-life was approximately 93 min. The signal gradually decreased in intensity up to the 360 min (6 h) time point (Figure 4B). In contrast, the signal of the ASO-Cy5.5 decreased more rapidly with a fluorescence signal half-life of approximately 43 s (Figure 4B). These results indicate that Phe-NPs/ASO-Cy5.5 was significantly more stable in systemic circulation than the naked ASO form.

Given the high fluorescence intensity observed in the head area following IV administration of Phe-NPs/ASO-Cy5.5, we quantified the cumulative fluorescence in the brain and expressed it as a percentage of the total injected dose per gram (%ID/g) of brain tissue. The analysis shows that the fluorescence intensity signal in the brain was increased by nearly 2-fold 90 min post-IV administration of Phe-NPs/ASO-Cy5.5 compared to that of ASO-Cy5.5 (ID%/g values of, respectively, 7.00% ± 0.82% and 0.11% ± 0.01%; $t_{(4)} = 8.281$, $p < 0.01$; Figure 4C).

To investigate the potential of Phe-NPs/ASO-Cy5.5 to cross the BBB in mice, we performed intravital confocal laser scanning microscopy (IV-CLSM) imaging, which allowed us to track the brain tissue penetration kinetics of Phe-NPs/ASO-Cy5.5 post-IV administration, and compared it with ASO-Cy5.5 molecules. In the latter, a Cy5.5 fluorescence signal was detected within the blood vessels for up to 10 min post-IV injection; no further fluorescence signal was evident at the 30-min time point (Figure 4D). In contrast, Phe-NPs/ASO-Cy5.5 exhibited a strong Cy5.5 fluorescence signal within blood vessels at 3 min post-IV injection of NPs, a signal that, impressively, increased gradually over time (Figure 4E). At the 30 min post-IV time point, the Cy5.5 fluorescence signal was detectable on the brain parenchyma side and was prolonged for up to 90 min post-IV injection (Figure 4E). These data demonstrate that circulating Phe-NPs/ASO-Cy5.5 effectively crossed the BBB into brain tissue in significant quantities.

Pharmacokinetics and biodistribution of Phe-NPs/ASO-Cy5.5 in non-human primate marmosets

Given the comparably high expression of LAT1 mRNA and protein in non-human primate (NHP) versus mouse brains, we sought to establish the biodistribution and proof of mechanism of Phe-NPs/ASO-Cy5.5 in the brain of an NHP species to lay the groundwork for the clinical translatability of this RNA-based NP medicine. Our data showed that following a 1 h IV infusion of Phe-NPs/ASO-Cy5.5 in a marmoset, a high fluorescence intensity signal was observed at the level of the brain 30 min post-IV infusion (Figure 5A). The relatively strong Cy5.5 fluorescence signal was sustained for up to 3 h post-IV infusion around the head area and was sustained for up to 72 h post-IV infusion (Figure 5A). Cy5.5 fluorescence was detected in the lungs and the liver. In the kidney, a relatively moderate Cy5.5 fluorescence signal was observed at early time points post-infusion, which increased gradually over time (Figure 5A), indicating that Phe-NPs/ASO-Cy5.5 were eliminated and excreted primarily via the renal route.

We further measured the fluorescence intensity signals in the cerebrospinal fluid (CSF) of the marmosets post-IV infusion of Phe-NPs/ASO-Cy5.5. Our data showed that the Cy5.5 signal significantly increased at the 2 h time point post-IV infusion by approximately 3.3-fold, compared to that at the baseline, measured prior to IV infusion (Figure 5B). While this signal gradually declined over time, it was still approximately 2-fold higher than the baseline, at the 6 h post-IV time point (Figure 5B).

Phe-NPs/ASO target knockdown in mouse brain

We further sought to determine whether the ASO cargo, which was effectively delivered to the brain tissue through its Phe-NPs/ASO, could effectively modulate its intended molecular target, miR-485-3p, within brain cells *in vivo*. Therefore, we determined the target gene expression levels in the brain using qPCR analysis following ICV or IV administration of Phe-NPs/ASO in mice. ICV-delivered Phe-NPs/ASO particles resulted in a significant dose-dependent knockdown of the target gene in all brain sub-regions investigated, including the cortex, striatum, thalamus, hippocampus, and midbrain (brain region: $F_{(9,90)} = 3.807$, $p < 0.001$; treatment: $F_{(2,90)} = 95.91$, $p < 0.0001$; interaction: $F_{(18,90)} = 1.224$, $p = 0.26$) (Figure 6A). Similarly, and impressively, to ICV, IV administration of Phe-NPs/ASO resulted in a significant dose-dependent knockdown of the target gene in all brain sub-regions investigated (brain region: $F_{(9,60)} = 1.664$, $p = 0.1180$; treatment: $F_{(2,60)} = 46.75$, $p < 0.0001$; interaction: $F_{(18,60)} = 0.6791$, $p = 0.8176$) (Figure 6B). Collectively, these data clearly demonstrate that our Phe-NPs/ASO, upon IV administration, can not only deliver a therapeutic ASO of choice through the BBB but it can also intracellularly reach brain cells *in situ*, releasing their RNA cargo via endosomal escape, for the ASO to induce pharmacologically relevant activity on a target of choice *in vivo*.

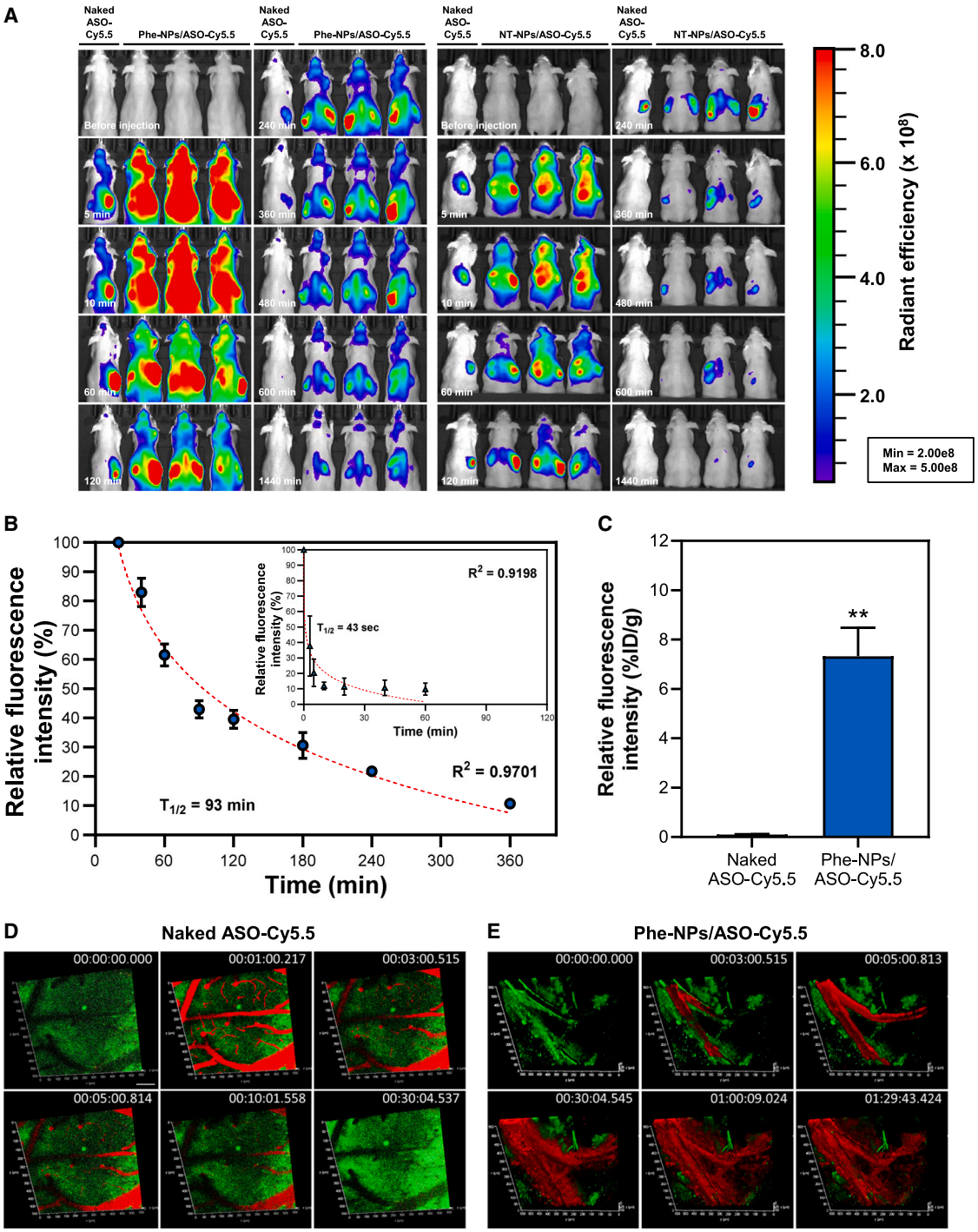

Figure 4. Pharmacokinetics, biodistribution, and BBB crossing of Phe-NPs/ASO-Cy5.5 in mouse

(A) *In vivo* fluorescence imaging of Hsd:ICR (CD-1) mice after 1.0 mg/kg IV administration of ASO-Cy5.5, Phe-NPs/ASO-Cy5.5, or NT-NPS/ASO-Cy5.5, for up to 24 h. (B) Pharmacokinetics of IV-administered ASO-Cy5.5 or Phe-NPs/ASO-Cy5.5 in blood. (C) Accumulated ASO in mouse brain, expressed as %ID/g, 90 min post-IV administration of 1.0 mg/kg of ASO-Cy5.5 or Phe-NPs/ASO-Cy5.5. Data are presented as means ± SDs (unpaired t test, $^{****}p < 0.001$ vs. naked ASO-Cy5.5). (D and E) IV-CLSM imaging, *in vivo* BBB crossing: ASO-Cy5.5 (D) and Phe-NPs/ASO-Cy5.5 in mouse brain (E). Scale bar: 100 μm.

DISCUSSION

NP-based platforms have a promising potential for delivering targeted RNA-based gene therapeutics, such as mRNA, ASO, siRNAs, and miRNAs, against a broad range of diseases, including neurodegenerative diseases.[46,47] In this study, we designed and functionally characterized a systemically deliverable LAT1-targeting NPs, Phe-NPs/ASO, using a therapeutic ASO as a test cargo that targets miR-485-3p, an miRNA implicated in neurodegenerative pathways within the CNS.[48,49] Size and morphology are essential parameters in nanomaterial design that influence the transport and adsorption of biomolecules, as well as their tissue biodistribution and subsequent cellular internalization *in vivo*.[50,51] In general, small spherical NPs feature a high surface-area-to-volume ratio, which facilitates greater drug cargo loading and surface modification for targeted delivery.[9,52] Moreover, small NPs may penetrate the BBB more efficiently, allowing drugs to reach the brain parenchymal cells more easily.[53,54] Very small NPs, <10–20 nm, may be subject to rapid renal clearance, and the size dispersion of NPs may negatively impact particle interactions with the target biological system.[55,56] Here, we developed a Phe-NPs/ASO system with the following optimal morphological features: a spherical shape, a size of 40 nm, BBB crossing idealness while retarding renal clearance, and a PDI of approximately 0.1. These findings suggest that Phe-NPs/ASO possesses ideal properties for targeted selectivity, BBB penetration, cellular adsorption, and intracellular delivery.

Stability and dissociation properties are key design parameters for NPs and their cargo to efficiently act on targeted biological systems. Our results demonstrate that Phe-NPs/ASO were highly stable *in vitro* under conditions mimicking the blood environment *in vivo*, as compared to a "naked" ASO control. PEG polymer chains have been used widely in the formulation of the outer layer of NPs and are known to enhance stability while maintaining blood circulation, biocompatibility, and water solubility.[57] These characteristics enable drug-carrying NPs to flow effectively through blood vessels, avoid rapid clearance, and reach the target tissues in higher quantities. Additionally, Phe-NPs/ASO exhibited GSH- and pH-dependent dissociation kinetics, with effective ASO drug cargo release via endosomal escape upon cellular internalization. GSH is a molecular species involved in cellular redox reactions. It usually remains at concentrations of 10 μM in the bloodstream but reaches 3 mM concentrations in various types of brain cells.[58–61] With endosomes exhibiting an acidic pH range of 5.0–6.0, efficient endosomal escape is essential for the cytosolic delivery of drug cargoes via internalized NPs.[62,63] Based on our design strategy and the resultant physicochemical properties of Phe-NPs/ASO, including GSH concentration and pH dependence, our delivery system-maintained stability in biofluids, such as blood, effectively reached the CNS and delivered pharmacologically active ASO drug cargo intracellularly through an endosomal escape process.

The conjugation of targeting moieties onto NPs is another design element of nanomedicines to enhance particle affinity toward specific cells or tissues.[64] The density of the targeting ligand moieties on the outer surface of NPs is a key control parameter in achieving optimal targeting and delivery to the tissue of interest, including the brain.[20,65] One study demonstrated that LAT1-targeting NPs exhibit substantially higher cellular uptake into glioblastoma cells than non-LAT1-targeting NPs.[41] Consistent with this finding, our results demonstrated that Cy5.5-labeled ASO-loaded NPs with 25%, 50%, 75%, or 100% Phe densities (Phe(25, 50, 75, and 100)-NPs/ASO-Cy5.5) showed higher cellular uptake efficiency in GL261-Luc cells, compared with those in an ASO-Cy5.5 control or with otherwise identical NPs without Phe ligand. These findings strongly suggest that LAT1 targeting is an efficient strategy to improve cellular uptake efficiency as well as the crossing of a LAT1-decorated tissue barrier, such as the BBB, of brain-targeting NPs. However, there were no discernible differences in cellular uptake based on variations in Phe ligand density in the 25%–100% range. Based on previous findings,[66,67] a saturation in cellular uptake efficiency was observed once a 25% Phe ligand density on the outer surface of NPs was reached. Additionally, the cellular uptake of NPs with 25% Phe density exhibited was significantly reduced in the presence of competitive Phe ligands (Figure 3B). Taken together, these findings indicated that our ASO-carrying NPs specifically targeted the LAT1 transporter, with a Phe ligand density of 25%. Notably, NT-NPs/ASO-Cy5.5 displayed a relatively higher cellular uptake than the ASO-Cy5.5 control *in vitro*. A likely interpretation is that the NPs conferred extra stability to their ASO cargo when present in the extracellular culture medium, thereby providing additional time for cellular uptake processes, while a portion of the particles might also have been taken up by LAT1-independent cellular uptake pathways.[41]

Most ASO-loaded nanomedicines developed to date rely solely on electrostatic stabilization, which makes them susceptible to dissociation *in vivo*. This instability typically leads to a short half-life while circulating in blood.[68] Achieving prolonged stability is essential for the effective accumulation of therapeutic molecules, such as ASOs, at pharmacologically active levels in targeted tissues.[69] In the present study, upon IV administration, Phe-NPs/ASO-Cy5.5 distributed in a robust and organ-wide fashion to the CNS of both mouse and higher-level species, such as NHP marmosets, compared with that of the ASO-Cy5.5 control or non-LAT1-targeting NT-NPs/ASO-Cy5.5 particles. The half-life of Phe-NPs/ASO-Cy5.5 particles in mouse blood was approximately 93 min, which is clear evidence of Phe-NPs/ASO particle superiority regarding stability under dynamic physiological conditions. In addition to this stability challenge, crossing the BBB represents another significant hurdle for successful NP delivery to the CNS.[68] Our IV-CLSM study demonstrated that Phe-NPs/ASO-Cy5.5 particles effectively crossed the BBB and broadly reached brain tissue regions. Specifically, significant accumulation of nanocarrier-delivered ASO-Cy5.5 in the brain was observed 90 min post-IV administration of Phe-NPs/ASO-Cy5.5 particles, which we approximated to 7.0% (%ID/g) of the total ID reaching the brain. A host of other NP-based drug delivery systems commonly achieve relatively low brain accumulation between 1.0% and 5.0% (%ID/g).[23–25] Furthermore, when IV administered, Phe-NPs/ASO demonstrated a significant knockdown effect on the miRNA target of ASO in all sub-regions of the brain that we investigated. Notably, the

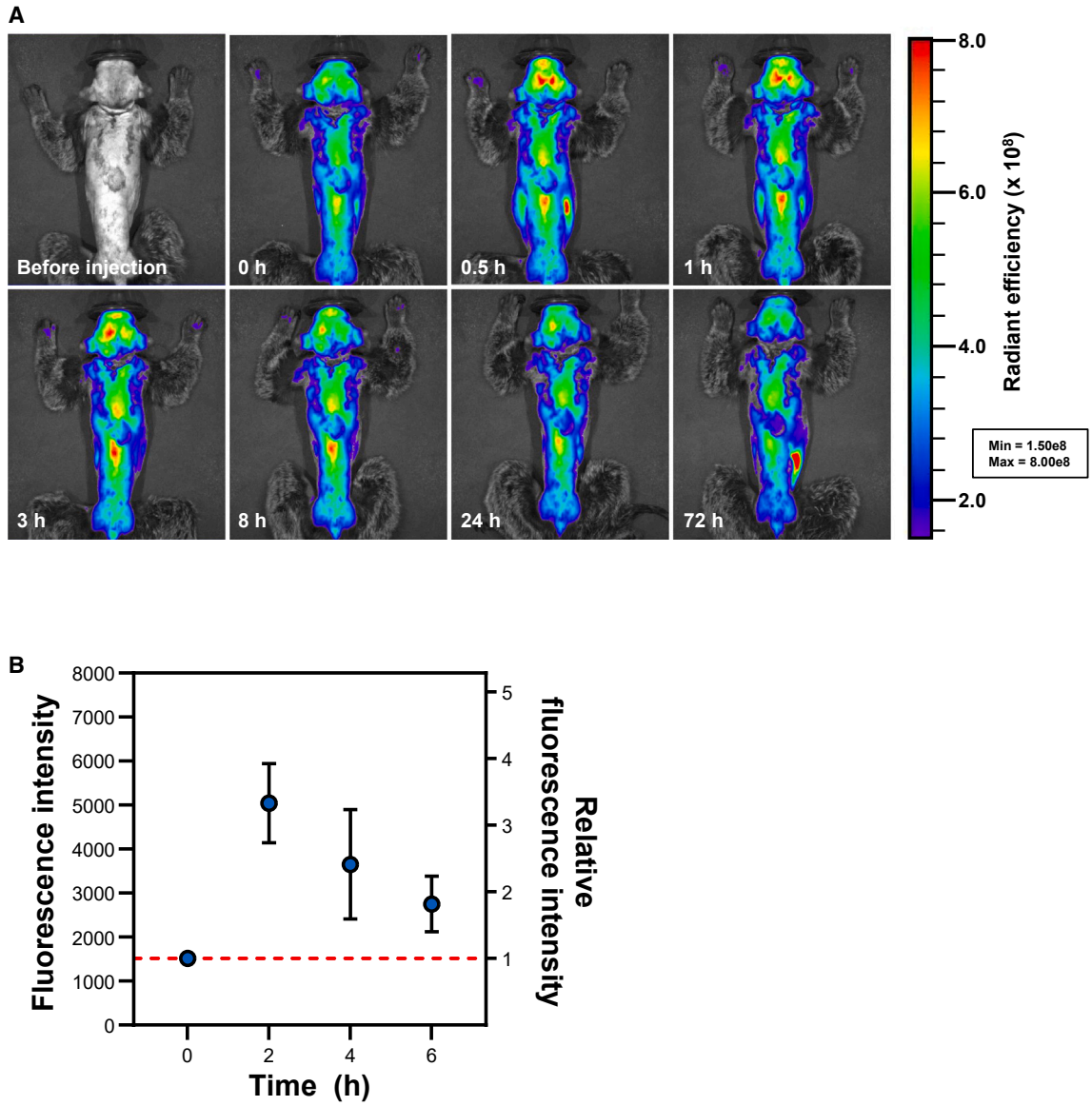

Figure 5. Biodistribution and pharmacokinetics of Phe-NPs/ASO-Cy5.5 in NHP

(A) Temporal changes in Cy5.5 fluorescence in marmoset, post-IV administration of Phe-NPs/ASO-Cy5.5. (B) Pharmacokinetics of IV-administered Phe-NPs/ASO-Cy5.5 in the CSF of cynomolgus monkeys.

knockdown effect exhibited a dose-dependent tendency similar to that observed when the same NPs were administered directly into the brain via the ICV route, achieving up to a 50% target gene knockdown. Overall, these results strongly suggest that our optimally designed NP delivery system effectively delivers its ASO target to a broad set of brain sub-regions with subsequent pharmacological activity against its intended miRNA target in brain cells following stability in the blood and effective crossing of the BBB after IV administration. In a higher-level species, such as NHP marmoset, the IV-delivered Phe-NPs/ASO particles consistently showed effective biodistribution in the CNS, with the ASO cargo being detected "downstream" in the CSF. Similar to NHP brains, the human brain also expresses high levels of LAT1 protein at the BBB and in various human brain cell types.[35]

In summary, we successfully developed a LAT1-targeting, RNA-based drug cargo NP with demonstrated brain accumulation of the drug cargo following non-invasive IV administration. The optimization of the Phe-NPs/ASO particle size and shape allowed for enhanced stability in blood circulation, while the addition of Phe ligand moieties on the outer surface of the particles significantly increased the selectivity and binding affinity to the LAT1 transporter

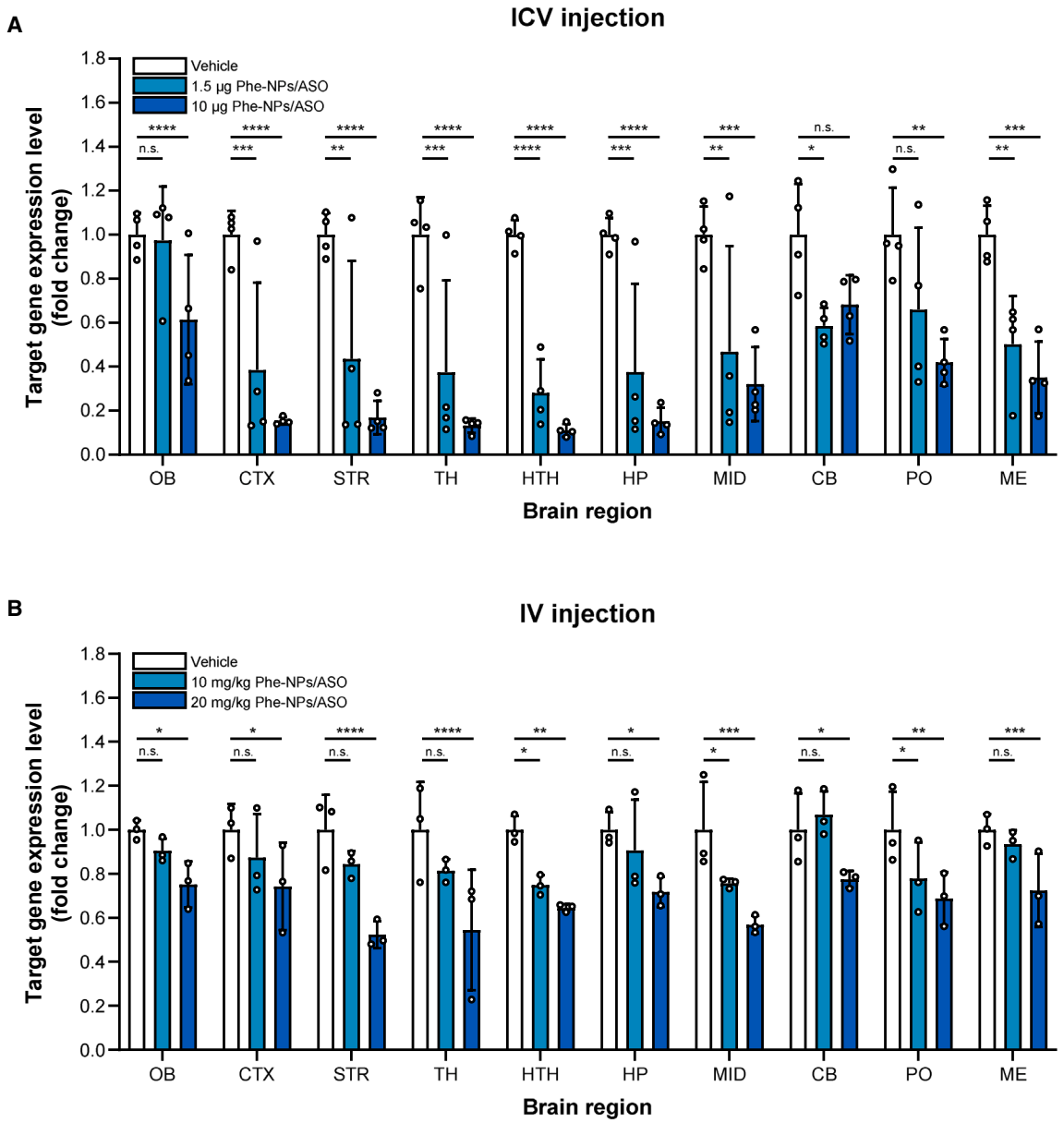

Figure 6. Phe-NPs/ASO target knockdown in sub-regions of mouse brain

(A) Target gene knockdown in sub-regions of mouse brain, 1 h post-ICV injection of 1.5 or 10 μg Phe-NPs/ASO. (B) Target gene knockdown in sub-regions of mouse brain, 30 min post-IV injection of 10 or 20 mg/kg of Phe-NPs/ASO. Data are presented as means ± SDs (one-way ANOVA and Tukey multiple comparison tests; $^{*}p < 0.05$; $^{**}p < 0.01$; $^{***}p < 0.001$; $^{****}p < 0.0001$). OB, olfactory bulb; CB, cerebellum; CTX, cortex; HP, hippocampus; HTH, hypothalamus; ME, medulla; MID, midbrain; PO, pons; STR, striatum; TH, thalamus; n.s., not significant.

expressed on BCECs, thereby facilitating efficient crossing of the BBB in rodent and NHP brains. Transporters such as glucose transporter 1 (GLUT1) and LAT1 may intracellularly uptake NPs via transporter-mediated transcytosis or endocytosis[17,20]; the detailed underlying mechanisms for NPs crossing the BBB may be explored in a future study. Unlike GLUT1, LAT1 expression is maintained under pathological conditions such as AD[36,38,70,71]; our LAT1-targeting Phe-NPs/ASO drug carrier system holds the potential for a broad range of brain drug delivery applications in numerous CNS diseases, including neurodegenerative diseases.

MATERIALS AND METHODS

Materials

The DTDPA, Tris(3-hydroxypropyltriazolylmethyl) amine, copper (II) sulfate, sodium ascorbate, and L-GSH were purchased from Sigma-Aldrich (St. Louis, MO). Nicotinic acid, NHS, EDC, and

DTT were purchased from Alfa Aesar (Thermo Fisher Scientific, Haverhill, MA). *N*-(*tert*-Butoxycarbonyl)-L-tyrosine methyl ether, propargyl bromide, and potassium carbonate were purchased from TCI Chemicals (Tokyo, Japan); α-methoxy-ω-amino poly(ethylene glycol)-*r*-poly-L-lysine (MeO-PEG-PLL(NH_3^+/Cl^-), MW = 18,094 Da) and azido-ω-amino PEG-PLL-NH_2 (N_3-PEG-PLL(NH_3^+/Cl^-), MW = 18,021 Da) were purchased from Alamanda Polymers (Huntsville, AL). HEPES solution (1 M) and HEPES powder for NPs formulation were purchased from Hyclone™ (Cytiva, Waltham, MA, USA) and Thermo Fisher Scientific, respectively. Nuclease-free water and the Quant-iT RiboGreen Assay Kit (R11490) were purchased from Qiagen (Hilden, Germany) and Invitrogen (Thermo Fisher Scientific), respectively.

Experimental methods

Preparation of Phe-NPs/ASO

NPs were prepared by mixing MeO-PEG-PLL(NA/MPA), a copolymer without any LAT1-targeting ligand, Phe-PEG-PLL(NA/MPA), and a copolymer amended with an LAT1-targeting ligand, all in solution with ASO molecules. Targeting and non-targeting copolymers were dissolved at a concentration of 8 mg/mL in a 200 mM DTT solution (10 mM HEPES buffer). Both copolymer solutions were mixed in a 3:1 v/v ratio. The ASO solution (180 μM) was prepared by dissolution in nuclease-free water.

The ASO and polymer solutions were then mixed in a 2:1 v/v ratio using a microfluidic mixer (Ignite, Precision NanoSystems [Cytiva], Vancouver, BC, Canada). The polymer-to-ASO mixing ratios were determined based on the optimized conditions for NP formation, including an amine (in polymer)-to-phosphate (in ASO) N-to-P ratio of 1.6. The mixture of ASO and polymer was kept at 25°C for 30 min for stabilization and then transferred to a dialysis cassette (MW cutoff of 20 kDa). Dialysis was conducted against a 5 mM HEPES and 5% DMSO solution for 1 day and in 5 mM HEPES for 2 days. After dialysis, the samples were filtered using a filter (0.22 μm polyethersulfone bottle top filter, Corning, Corning, NY) and lyophilized with cryoprotectant (mannitol and sucrose, 1:4 v/v). Lyophilized powder of Phe-NPs/ASO was stored at −20°C prior to use. The size distribution of NPs was measured using a Zetasizer (ZS and Ultra Red, Malvern Panalytical, Malvern, UK). Cryo-TEM images were acquired using a 300-kV cryo-biotransmission electron microscope with high-resolution structural capabilities (Krios G4 Cryo-TEM, Thermo Fisher Scientific, at the Institute for Basic Science, Daejeon, South Korea).

Characterization of NPs

Encapsulation efficiency by Quant-iT RiboGreen Assay

Typically, the RiboGreen assay method is used to confirm the RNA content within lipid NPs. In this study, we aimed to obtain the ASO content and EE% within polyion complex micelles by using a modified method of the RiboGreen assay. The experiment was conducted according to the protocol provided by the manufacturer. For the measurement, the ASO concentration in the NPs was diluted to 2 μg/mL with Tris-ethylenediaminetetraacetic acid (Tris-EDTA [TE]) buffer, and 50 μL was transferred to a black 96 well plate. To measure EE%, 50 μL TE 1× buffer or 0.2% dextran sulfate (MW 5,000, TdB Labs, Uppsala, Sweden) solution was added. The standard curve was prepared by mixing 50 μL ASO solutions at concentrations of 0.4, 1, 2, 4, and 125 μg/mL (in TE buffer) with 50 μL 0.2% dextran sulfate solution and transferring them to the plate. The plate was incubated at 37°C for 15 min. Then, 100 μL RiboGreen diluted 1:100 % v/v was added to each well, and the fluorescence intensity was measured using a microplate reader (Infinite M Plex, TECAN, Maennedorf, Switzerland) at excitation wavelength/emission wavelength (Ex/Em) = 480/525. The measurements were performed in technical triplicate ($N = 3$).

Stability test

For the stability study of Phe-NPs/ASO against GSH and pH, GSH solution was prepared by dissolving in 10 mM HEPES buffer (pH 7.10) at different concentrations of 0.1, 1.0, 10, and 100 mM, and different pHs of HEPES buffer (pH 5.28 and pH 7.10) were prepared. After dissolving the Phe-NPs/ASO in nuclease-free water (150 μM ASO concentration), NP solution was mixed with each GSH solution or HEPES in a 1:9 v/v ratio. Then, the mixture was incubated for 30 min at 25°C. The stability of the NPs was assessed by measuring the total particle number concentration of NPs using a Zetasizer (ZS and Ultra Red).

In vitro studies

Cell culture

GL261-Luc cells, a glioma cell line, was used as an *in vitro* model of cells expressing LAT1. GL261-Luc cells were cultured in DMEM supplemented with 10% fetal bovine serum and 1% penicillin, in a 95% O_2/5% CO_2 incubator at 37°C.

Cell uptake and flow cytometry assays

Flow cytometry was performed as previously described.[20] GL261-Luc cells were seeded at a density of 5×10^4 cells per well in a 24 well plate and incubated at 37°C, 95% O_2/5% CO_2, for 24 h. Cells were then incubated with PBS and either ASO-Cy5.5 or ASO-Cy5.5 with varying ligand densities (0%, 25%, 50%, 75%, and 100%). A target concentration of 7.5 μM of either the ASO-Cy5.5 or the NPs with varying ligand densities was obtained in 20 μL PBS and upon re-dispersion in 480 μL of culture medium. The prepared samples were then added to the appropriate wells; wells were incubated at 37°C, 95% O_2/5% CO_2, for 30 min. Cells were subsequently digested using 0.25% w/v trypsin-EDTA and treated culture medium. The cell suspensions were collected and centrifuged at 1,000 rpm for 2 min. Upon centrifugation, the suspensions were washed twice with PBS and re-suspended in 200 μL PBS. Using a BD Accuri C6 Plus (Becton Dickinson, Franklin Lakes, NJ) flow cytometer, cell numbers and Cy5.5 fluorescence intensities were measured. Fluorescence data of live cells were ultimately captured, based on 15,000 gated events, using the BD CSampler Plus (Becton Dickinson).

Cell-based assay for ASO-loaded NPs uptake

To investigate the ability of Phe to target LAT1, we performed a competition assay using GL261-Luc cells. The cellular uptake of

NT-NPs/ASO-Cy5.5 and Phe-NPs/ASO-Cy5.5 was compared in the presence or absence of free Phe. Briefly, cells were cultured in a 96 well plate at a seeding density of 5×10^3 cells per well. At 24 h post-seeding, the cells were washed in cell culture medium and the selected wells were treated with 10 μL LAT1 ligand, Phe (1 mM in cell culture medium); other wells were given an additional 10 μL cell culture medium. The 96 well plate treated with ligands was then placed at 37°C in the CO_2 incubator for an additional hour. NT-NPs/ASO-Cy5.5 or Phe-NPs/ASO-Cy5.5 (20 μL) was then added at a total ASO concentration of 300 nM/well, and 20 μL PBS was added into another well as a non-treated control. The 96 well plate was transferred back to the incubator for an additional hour to allow cellular uptake of the ASO-loaded NPs. The cell culture medium was subsequently removed, and the cells were washed three times with PBS. After a final addition of 100 μL PBS to each well, cell fluorescence was measured using a microplate reader (Ex/Em = 650/690 nm). The measured fluorescence intensity of the NP treatment group was subtracted from that of the untreated control.

Cell-based assay for endosomal escape analysis

Endosomal escape imaging was performed as previously described.[72] Briefly, GL261-Luc cells were seeded at a density of 3×10^3 cells per dish on glass coverslip plates and incubated for 24 h at 37°C, 95% O_2/5% CO_2, conditions. Cells were then washed twice with PBS, exposed to Phe-NPs/ASO-Cy5.5 at a total ASO concentration of 300 nM, and incubated again at 37°C, 95% O_2/5% CO_2, for 1 h. Cells were then washed twice with PBS, and dishes were filled with culture medium and incubated at 37°C for 0, 1, 2, or 4 h. The cells were washed again with PBS at the predetermined times. The cells were then treated with 75 nM LysoTracker (Invitrogen) for 3 min, and cell nuclei were stained with Hoechst dye 33342 (6-min exposure time). Cells were ultimately washed three times with PBS and fixed with 4% paraformaldehyde for 10 min. Confocal images were acquired using a Leica confocal microscope (STELLARIS 5 *in vivo* confocal system, Leica Microsystems, Wetzlar, Germany), and Cy5.5-labeled cells were analyzed using companion imaging software (Leica Application Suite X, Leica Microsystems). The region of interest intensities of each color in the confocal images were analyzed by ImageJ. In brief, the red and colocalized yellow signals were analyzed by setting color thresholds for each color. The mean intensities of each color were analyzed in five different cells selected at each time point.

In vivo studies in mouse

Animals

Hsd:ICR (CD-1) mice were purchased from Koatech (Pyeongtaek, South Korea). The Hsd:ICR mice originated from the Charles River Laboratories (Wilmington, MA). C57BL/6J mice were purchased from DBL (Eumseong, South Korea) and obtained from Jackson Laboratory (Bar Harbor, ME). The animal studies were approved by the Institutional Animal Care and Use Committee (IACUC) at BIORCHESTRA (approval nos. BOIACUC-20220215-0001, BOIACUC-20220215-0003, and BOIACUC-20220218-0001). All procedures related to the animal studies outlined in this paper strictly adhered to the guidelines set forth by the IACUC for animal care. All mice were housed under controlled conditions, with a fixed temperature of 20°C ± 1°C and a relative humidity of 25% ± 10%, under 12 h light/dark cycles.

For the NHP marmoset study, NP drug sample administration and in-life biological sampling were conducted at either KBIO Health (approval no. KBIO-IACUC-2020-145) or KRIBB (approval nos. KRIBB-AEC-20263 and KRIBB-AEC-22127); biosample analyses, such as fluorescence intensities based on blood and CSF samples, were conducted at BIORCHESTRA.

Biodistribution in mouse

We investigated the biodistribution of Phe-NPs/ASO (with Cy5.5-labeled ASO) in the mouse following tail vein administration, using a live *in vivo* imaging system (IVIS) imaging method (IVIS Lumina LT Series III, Revvity, Waltham, MA). Hair on the backs and heads of the animals was shaved off prior to recording the IVIS images. The injection amount of NT-NPs/ASO-Cy5.5 and Phe-NPs/ASO-Cy5.5 in mice was set at a total ASO dose of 25 μg in 200 μL PBS (0.125 mg/mL ASO concentration). As a negative control, unformulated ASO-Cy5.5 was dissolved in PBS and fluorescence intensity was adjusted to NPs/ASO-Cy5.5 by dilution with PBS to avoid saturation of the fluorescence imaging in IVIS. One mouse per study group was administered the ASO-Cy5.5. Three mice per group were administered the non-LAT1-targeting NT-NPs/ASO-Cy5.5; another three mice per group were given the LAT1-targeting Phe-NPs/ASO-Cy5.5. IVIS imaging was then performed at pre-set time points of 5, 10, and 30 min and at 1, 2, 4, 6, 8, 12, and 24 h. The imaging data were processed using Living Image Software version 4.7.2 (Revvity).

Blood samples

The 200 μL PCR tubes were pre-conditioned with 10 μL of an anticoagulant, 3.2% sodium citrate solution. Mice were administered, via tail vein injection, ASO-Cy5.5 or Phe-NPs/ASO-Cy5.5 (containing 25 μg ASO amount, 0.125 mg/mL, $N = 3$ per group). Then, 20 μL of arterial blood was drawn at pre-set time points of 30 min, 1, 2, 4, 6, 8, 12, and 24 h. The collected blood was immediately placed in pre-conditioned PCR tubes, mixed, and stored on ice. Lysis buffer (30 μL) was added to each tube immediately after blood collection at all time points. The mixture solutions of 50 μL/tube were next transferred to a black 96 well plate. Fluorescence intensities were measured (Ex/Em = 650/690 nm) using a microplate reader (SpectraMax iD3; Molecular Devices, San Jose, CA).

Quantification of ASO delivery to the brain

We quantified the amount of fluorescence-labeled ASO materials delivered via nanocarriers to the brain tissue, as described previously.[20] The amount of Phe-NPs/ASO-Cy5.5 was detected by measuring the Cy5.5 fluorescence intensities in brain tissue slices. Six-week-old male Hsd:ICR mice ($N = 3$) were IV injected with either Phe-NPs/ASO-Cy5.5 (containing 25 μg of ASO amount, 0.125 mg/mL) or PBS as a negative control. Mice were sacrificed 1.5 h after injection. Whole brains were dissected after perfusion

with PBS. Half of each brain was immediately weighed and homogenized using a multi-bead shocker (TissueLyser II, Qiagen) with 600 μL lysis buffer (Passive Lysis buffer 5×; Promega, Madison, WI). Brain lysates were then centrifuged at 5,000 rpm for 10 min, and the supernatants were transferred to a black 96 well plate. Cy5.5 fluorescence intensities were measured (Ex/Em = 650/690 nm) using a microplate reader (SpectraMax iD3; Molecular Devices).

IV-CLSM

IV-CLSM was performed as previously described.[65] Mice were anesthetized with 2.5% isoflurane (ISOTROY 100, Troikaa Pharmaceuticals, Ahmedabad, India) during the experimental process. A 3- to 5-mm diameter hole was drilled into the skull. A glass coverslip was then placed on the brain. After fixing the head of the mouse in a steady position, the microscope lens was focused on the brain tissue and blood capillaries, which were accessible through a glass coverslip. Phe-NPs/ASO-Cy5.5 or ASO-Cy5.5 were IV injected (containing 25 μg of ASO amount, 0.125 mg/mL) into 6-week-old male Hsd:ICR mice, and Cy5.5 fluorescence intensities were measured using an IV-CLSM system (STELLARIS, Leica). Time-dependent fluorescence intensities of Cy5.5 (Ex/Em = 640/662–738 nm) were observed at the surface of the brains of mice for 90 min. Images were recorded every 30 s.

Target knockdown in tissue: RNA extraction and qPCR analysis

RNA extraction and qPCR analyses were performed as previously described.[48,73] Total RNA was extracted from brain sub-regions using Trizol reagent (Invitrogen) according to the Direct-zol RNA Miniprep Plus instructions (Zymo Research, Irvine, CA). A miScript II RT Kit (Qiagen) was used for cDNA synthesis. Expression levels of the ASO target, the miR-485-3p miRNA, were measured using qPCR with a Bio-Rad CFX real-time PCR system (Bio-Rad, Hercules, CA) and the TOPreal Probe qPCR PreMIX (Enzynomics, Daejeon, South Korea), according to the manufacturers' instructions. The expression of RNU6 was used as an internal control. Relative expression levels of miR-485-3p were calculated using the $2^{-\Delta\Delta Ct}$ method and normalized to RNU6.

In vivo study in NHP

Biodistribution in marmoset

To investigate the biodistribution of Phe-NPs/ASO-Cy5.5 in marmoset, a live imaging method was implemented using ASO-Cy5.5. The hair on the back and head of the marmosets was shaved off prior to IVIS imaging measurements. The fluorescence intensities of ASO-Cy5.5 and Phe-NPs/ASO-Cy5.5 were adjusted to the same initial fluorescence intensity baselines. Marmosets were administered either ASO-Cy5.5 or Phe-NPs/ASO-Cy5.5 (containing 0.255 mg of ASO amount, 0.125 mg/mL of ASO concentration; $N = 1$ per group) through the tail vein. IVIS images were subsequently acquired at preset time points of 0 and 30 min and at 1, 2, 3, 5, 8, 24, 48, and 72 h post-1 h IV infusion (infusion rate: 2.0 mL/h). The data were processed using Living Image Software version 4.7.2.

CSF biosampling and analyses in cynomolgus monkey

Cynomolgus monkeys received an IV infusion of Phe-NPs/ASO-Cy5.5 (containing 2.75 mg of ASO amount, 0.125 mg/mL of ASO concentration, $N = 1$ per group). At 10, 30, 120, and 360 min post-1 h IV infusion (infusion rate: 20 mL/h), CSF samples were collected in tubes. The CSF was collected sequentially in two independent vials at each time point post-IV infusion to minimize the risk of contamination during CSF collection. To determine fluorescence intensities, cynomolgus monkey CSF (30 μL) and lysis buffer (1×, 30 μL) were placed in a 0.2 mL PCR tube and vortexed; 50 μL of the mixture was then titrated and transferred to a 96 well plate, and 5 μL of an SDS solution (5%, diluted with RNase-free water) was added to each well and incubated at room temperature for 2 h. Samples were measured at Ex/Em = 650/690 nm using the microplate reader (SpectraMax iD3, Molecular Devices). Relative fluorescence intensities over time were calculated using the following method based on the basal intensity in the CSF before IV administration of Phe-NPs/ASO-Cy5.5.

ASO target knockdown study in mouse

Male C57BL/6J mice were used to quantify ASO target knockdown across brain regions *in vivo* following ICV or IV administration of Phe-NPs/ASO. Animals were housed in groups of four to five, at controlled temperature (23°C ± 1.0°C) and humidity (30%–70%), under regular 12 h light-dark cycles (light on at 8:00 a.m.). Two distinct studies were conducted, depending on the route of administration of the Phe-NPs/ASO: study 1 was performed under a single ICV administration of the NPs; study 2 used a single IV administration.

In study 1 (ICV), mice were anesthetized with 250 mg/kg 2,2,2-tribromoethanol (Sigma-Aldrich) in 2-methyl-2-butanol (Sigma-Aldrich) via intraperitoneal (IP) injection (10 mL/kg). The mice were placed in a stereotaxic apparatus (Kopf Instruments, Tujunga, CA). Under aseptic conditions, the Phe-NPs/ASO solution (1.5 or 10 μg, dissolved in PBS) was infused into the right lateral ventricle (0.5 mm anterior to bregma, 1.0 mm right of midline, and 2.5 mm below the skull surface) with a 10-μL Hamilton microsyringe (infusion volume: 5 μL, infusion rate: 0.5 μL/min).[48] Upon completion of the injection, the delivery needle was held in place for an additional 5 min to reduce the risk of backflow of the Phe-NPs/ASO or vehicle solution. The drilled hole was sealed with dental cement, and the wounded skin was fixed with autoclips. The brain and spinal cord were extracted. The brain was dissected into 10 sub-regions: olfactory bulb, cortex, striatum, thalamus, hypothalamus, hippocampus, midbrain, cerebellum, pons, and medulla. The spinal cord was dissected into cervical, thoracic, and lumbar cord sub-regions. The collected tissues were stored in a freezer until further analysis.

In study 2 (IV), mice were implanted with an indwelling jugular catheter (25G, polyurethane tubing; Instech Laboratories, Plymouth Meeting, PA) placed in the right jugular vein under anesthesia with 250 mg/kg 2,2,2-tribromoethanol (Sigma-Aldrich) in 2-methyl-2-butanol (Sigma-Aldrich) via IP injection (10 mL/kg). Catheter

patency was confirmed with a gentle 0.2 mL heparinized saline (30 IU/mL) push. Phe-NPs/ASO (10 or 20 mg/kg total ASO dose, 5 mL/kg) were administered to the mice through a catheter. Thirty minutes after IV administration of NPs, the mice were sacrificed for brain and spinal cord tissue collection. The detailed tissue collection processes were identical to those described in study 1 (ICV).

Statistical analyses

All statistical analyses were performed using GraphPad Prism version 10.0.2 (GraphPad Software, La Jolla, CA) and R statistical package, version 4.1.2 (R Foundation for Statistical Computing, Vienna, Austria). All data are presented as means ± SDs. The statistical significance between groups was determined using a two-tailed unpaired t test. Tukey's post hoc test was used for all one-way ANOVAs with repeated measures. Bonferroni's post hoc test was used for all repeated measures and two-way ANOVAs. The level of statistical significance was set at $p < 0.05$.

DATA AND CODE AVAILABILITY

The data generated and analyzed in the context of the present study are available from the corresponding author upon reasonable request.

ACKNOWLEDGMENTS

We thank members of the BIORCHESTRA Corporation for their valuable comments and suggestions. Special thanks to Dr. Youngjeon Lee and Dr. Hyeon-Gu Yeo from the National Primate Research Center of KRIBB for generously providing the brain sections of cynomolgus monkeys. This work was supported by the Technology Development Program (RS-2023-00283779) funded by the Ministry of SMEs and Startups (MMS, South Korea).

AUTHOR CONTRIBUTIONS

Y.N.L.: formal analysis, investigation, methodology, writing – original draft, writing – review & editing. I.S.R.: formal analysis, investigation, methodology, writing – original draft, writing – review & editing. Y.-J.J.: formal analysis, visualization, writing – original draft, writing – review & editing. G.H.: data interpretation, writing – review & editing. I.K.: investigation, methodology. H.W.P.: investigation. H.K.: investigation. J.L.: investigation. H.J.L.: investigation, methodology. K.S. Lee: formal analysis, resources. H.-N.J.: formal analysis, resources. D.-I.H.: investigation. J.P.: investigation. J.W.: investigation. K.S. Lim: investigation. C.-Y.J.: investigation. H.-J.C.: conceptualization, supervision. H.S.M.: conceptualization, methodology, project administration, supervision, writing – review & editing. J.-H.R.: conceptualization, funding acquisition, project administration, supervision, writing – review & editing.

DECLARATION OF INTERESTS

The authors confirm that they are employed and are paid by BIORCHESTRA Co., Ltd. The company had no direct or indirect interests in the preparation of the research paper.

SUPPLEMENTAL INFORMATION

Supplemental information can be found online at https://doi.org/10.1016/j.omtn.2024.102340.

REFERENCES

1. Bennett, C.F., Krainer, A.R., and Cleveland, D.W. (2019). Antisense Oligonucleotide Therapies for Neurodegenerative Diseases. Annu. Rev. Neurosci. *42*, 385–406. https://doi.org/10.1146/annurev-neuro-070918-050501.

2. Mendonca, M.C.P., Kont, A., Aburto, M.R., Cryan, J.F., and O'Driscoll, C.M. (2021). Advances in the Design of (Nano)Formulations for Delivery of Antisense Oligonucleotides and Small Interfering RNA: Focus on the Central Nervous System. Mol. Pharm. *18*, 1491–1506. https://doi.org/10.1021/acs.molpharmaceut.0c01238.

3. Monine, M., Norris, D., Wang, Y., and Nestorov, I. (2021). A physiologically-based pharmacokinetic model to describe antisense oligonucleotide distribution after intrathecal administration. J. Pharmacokinet. Pharmacodyn. *48*, 639–654. https://doi.org/10.1007/s10928-021-09761-0.

4. MacCannell, D., Berger, Z., Kirschner, J., Mercuri, E., Farrar, M.A., Iannaccone, S.T., Kuntz, N.L., Finkel, R.S., Valente, M., and Muntoni, F. (2022). Restoration of Nusinersen Levels Following Treatment Interruption in People With Spinal Muscular Atrophy: Simulations Based on a Population Pharmacokinetic Model. CNS Drugs *36*, 181–190. https://doi.org/10.1007/s40263-022-00899-0.

5. Holm, A., Hansen, S.N., Klitgaard, H., and Kauppinen, S. (2022). Clinical advances of RNA therapeutics for treatment of neurological and neuromuscular diseases. RNA Biol. *19*, 594–608. https://doi.org/10.1080/15476286.2022.2066334.

6. Zhao, Z., and Zlokovic, B.V. (2020). Therapeutic TVs for Crossing Barriers in the Brain. Cell *182*, 267–269. https://doi.org/10.1016/j.cell.2020.06.041.

7. Wu, D., Chen, Q., Chen, X., Han, F., Chen, Z., and Wang, Y. (2023). The blood-brain barrier: structure, regulation, and drug delivery. Signal Transduct. Targeted Ther. *8*, 217. https://doi.org/10.1038/s41392-023-01481-w.

8. Zuchero, Y.J.Y., Chen, X., Bien-Ly, N., Bumbaca, D., Tong, R.K., Gao, X., Zhang, S., Hoyte, K., Luk, W., Huntley, M.A., et al. (2016). Discovery of Novel Blood-Brain Barrier Targets to Enhance Brain Uptake of Therapeutic Antibodies. Neuron *89*, 70–82. https://doi.org/10.1016/j.neuron.2015.11.024.

9. Pinheiro, R.G.R., Coutinho, A.J., Pinheiro, M., and Neves, A.R. (2021). Nanoparticles for Targeted Brain Drug Delivery: What Do We Know? Int. J. Mol. Sci. *22*, 11654. https://doi.org/10.3390/ijms222111654.

10. Jones, A.R., and Shusta, E.V. (2007). Blood-brain barrier transport of therapeutics via receptor-mediation. Pharm. Res. (N.Y.) *24*, 1759–1771. https://doi.org/10.1007/s11095-007-9379-0.

11. Chew, K.S., Wells, R.C., Moshkforoush, A., Chan, D., Lechtenberg, K.J., Tran, H.L., Chow, J., Kim, D.J., Robles-Colmenares, Y., Srivastava, D.B., et al. (2023). CD98hc is a target for brain delivery of biotherapeutics. Nat. Commun. *14*, 5053. https://doi.org/10.1038/s41467-023-40681-4.

12. Li, J., Yang, H., Zhang, Y., Jiang, X., Guo, Y., An, S., Ma, H., He, X., and Jiang, C. (2015). Choline Derivate-Modified Doxorubicin Loaded Micelle for Glioma Therapy. ACS Appl. Mater. Interfaces *7*, 21589–21601. https://doi.org/10.1021/acsami.5b07045.

13. Su, H., Wang, Y., Liu, S., Wang, Y., Liu, Q., Liu, G., and Chen, Q. (2019). Emerging transporter-targeted nanoparticulate drug delivery systems. Acta Pharm. Sin. B *9*, 49–58. https://doi.org/10.1016/j.apsb.2018.10.005.

14. Kou, L., Hou, Y., Yao, Q., Guo, W., Wang, G., Wang, M., Fu, Q., He, Z., Ganapathy, V., and Sun, J. (2018). L-Carnitine-conjugated nanoparticles to promote permeation across blood-brain barrier and to target glioma cells for drug delivery via the novel organic cation/carnitine transporter OCTN2. Artif. Cells, Nanomed. Biotechnol. *46*, 1605–1616. https://doi.org/10.1080/21691401.2017.1384385.

15. Abdul Razzak, R., Florence, G.J., and Gunn-Moore, F.J. (2019). Approaches to CNS Drug Delivery with a Focus on Transporter-Mediated Transcytosis. Int. J. Mol. Sci. *20*, 3108. https://doi.org/10.3390/ijms20123108.

16. Mazumdar, S., Chitkara, D., and Mittal, A. (2021). Exploration and insights into the cellular internalization and intracellular fate of amphiphilic polymeric nanocarriers. Acta Pharm. Sin. B *11*, 903–924. https://doi.org/10.1016/j.apsb.2021.02.019.

17. Gyimesi, G., and Hediger, M.A. (2023). Transporter-Mediated Drug Delivery. Molecules *28*, 1151. https://doi.org/10.3390/molecules28031151.

18. Abbott, N.J., Rönnbäck, L., and Hansson, E. (2006). Astrocyte-endothelial interactions at the blood-brain barrier. Nat. Rev. Neurosci. *7*, 41–53. https://doi.org/10.1038/nrn1824.

19. Chen, Y., and Liu, L. (2012). Modern methods for delivery of drugs across the blood-brain barrier. Adv. Drug Deliv. Rev. *64*, 640–665. https://doi.org/10.1016/j.addr.2011.11.010.

20. Min, H.S., Kim, H.J., Naito, M., Ogura, S., Toh, K., Hayashi, K., Kim, B.S., Fukushima, S., Anraku, Y., Miyata, K., and Kataoka, K. (2020). Systemic Brain Delivery of Antisense Oligonucleotides across the Blood-Brain Barrier with a Glucose-Coated Polymeric Nanocarrier. Angew. Chem., Int. Ed. Engl. *59*, 8173–8180. https://doi.org/10.1002/anie.201914751.

21. Somani, S., Blatchford, D.R., Millington, O., Stevenson, M.L., and Dufès, C. (2014). Transferrin-bearing polypropylenimine dendrimer for targeted gene delivery to the brain. J. Contr. Release *188*, 78–86. https://doi.org/10.1016/j.jconrel.2014.06.006.

22. Zhang, Y., Schlachetzki, F., and Pardridge, W.M. (2003). Global non-viral gene transfer to the primate brain following intravenous administration. Mol. Ther. *7*, 11–18. https://doi.org/10.1016/s1525-0016(02)00018-7.

23. Pandit, R., Chen, L., and Götz, J. (2020). The blood-brain barrier: Physiology and strategies for drug delivery. Adv. Drug Deliv. Rev. *165–166*, 1–14. https://doi.org/10.1016/j.addr.2019.11.009.

24. Patra, J.K., Das, G., Fraceto, L.F., Campos, E.V.R., Rodriguez-Torres, M.D.P., Acosta-Torres, L.S., Diaz-Torres, L.A., Grillo, R., Swamy, M.K., Sharma, S., et al. (2018). Nano based drug delivery systems: recent developments and future prospects. J. Nanobiotechnol. *16*, 71. https://doi.org/10.1186/s12951-018-0392-8.

25. Banks, W.A. (2016). From blood-brain barrier to blood-brain interface: new opportunities for CNS drug delivery. Nat. Rev. Drug Discov. *15*, 275–292. https://doi.org/10.1038/nrd.2015.21.

26. Terstappen, G.C., Meyer, A.H., Bell, R.D., and Zhang, W. (2021). Strategies for delivering therapeutics across the blood-brain barrier. Nat. Rev. Drug Discov. *20*, 362–383. https://doi.org/10.1038/s41573-021-00139-y.

27. Ni, M., Xiong, M., Zhang, X., Cai, G., Chen, H., Zeng, Q., and Yu, Z. (2015). Poly(lactic-co-glycolic acid) nanoparticles conjugated with CD133 aptamers for targeted salinomycin delivery to CD133+ osteosarcoma cancer stem cells. Int. J. Nanomed. *10*, 2537–2554. https://doi.org/10.2147/IJN.S78498.

28. Shi, P., Cheng, Z., Zhao, K., Chen, Y., Zhang, A., Gan, W., and Zhang, Y. (2023). Active targeting schemes for nano-drug delivery systems in osteosarcoma therapeutics. J. Nanobiotechnol. *21*, 103. https://doi.org/10.1186/s12951-023-01826-1.

29. Ikotun, O.F., Marquez, B.V., Huang, C., Masuko, K., Daiji, M., Masuko, T., McConathy, J., and Lapi, S.E. (2013). Imaging the L-type amino acid transporter-1 (LAT1) with Zr-89 immunoPET. PLoS One *8*, e77476. https://doi.org/10.1371/journal.pone.0077476.

30. Scalise, M., Galluccio, M., Console, L., Pochini, L., and Indiveri, C. (2018). The Human SLC7A5 (LAT1): The Intriguing Histidine/Large Neutral Amino Acid Transporter and Its Relevance to Human Health. Front. Chem. *6*, 243. https://doi.org/10.3389/fchem.2018.00243.

31. Barar, J., Rafi, M.A., Pourseif, M.M., and Omidi, Y. (2016). Blood-brain barrier transport machineries and targeted therapy of brain diseases. Bioimpacts *6*, 225–248. https://doi.org/10.15171/bi.2016.30.

32. Yan, R., Li, Y., Müller, J., Zhang, Y., Singer, S., Xia, L., Zhong, X., Gertsch, J., Altmann, K.H., and Zhou, Q. (2021). Mechanism of substrate transport and inhibition of the human LAT1-4F2hc amino acid transporter. Cell Discov. *7*, 16. https://doi.org/10.1038/s41421-021-00247-4.

33. Kanai, Y. (2022). Amino acid transporter LAT1 (SLC7A5) as a molecular target for cancer diagnosis and therapeutics. Pharmacol. Ther. *230*, 107964. https://doi.org/10.1016/j.pharmthera.2021.107964.

34. Pardridge, W.M. (2022). A Historical Review of Brain Drug Delivery. Pharmaceutics *14*, 1283. https://doi.org/10.3390/pharmaceutics14061283.

35. Yanagida, O., Kanai, Y., Chairoungdua, A., Kim, D.K., Segawa, H., Nii, T., Cha, S.H., Matsuo, H., Fukushima, J., Fukasawa, Y., et al. (2001). Human L-type amino acid transporter 1 (LAT1): characterization of function and expression in tumor cell lines. Biochim. Biophys. Acta *1514*, 291–302. https://doi.org/10.1016/s0005-2736(01)00384-4.

36. Barthelemy, C., and André, B. (2019). Ubiquitylation and endocytosis of the human LAT1/SLC7A5 amino acid transporter. Sci. Rep. *9*, 16760. https://doi.org/10.1038/s41598-019-53065-w.

37. Zhang, J., Xu, Y., Li, D., Fu, L., Zhang, X., Bao, Y., and Zheng, L. (2020). Review of the Correlation of LAT1 With Diseases: Mechanism and Treatment. Front. Chem. *8*, 564809. https://doi.org/10.3389/fchem.2020.564809.

38. Huttunen, J., Peltokangas, S., Gynther, M., Natunen, T., Hiltunen, M., Auriola, S., Ruponen, M., Vellonen, K.S., and Huttunen, K.M. (2019). L-Type Amino Acid Transporter 1 (LAT1/Lat1)-Utilizing Prodrugs Can Improve the Delivery of Drugs into Neurons, Astrocytes and Microglia. Sci. Rep. *9*, 12860. https://doi.org/10.1038/s41598-019-49009-z.

39. Puris, E., Saveleva, L., de Sousa Maciel, I., Kanninen, K.M., Auriola, S., and Fricker, G. (2023). Protein Expression of Amino Acid Transporters Is Altered in Isolated Cerebral Microvessels of 5xFAD Mouse Model of Alzheimer's Disease. Mol. Neurobiol. *60*, 732–748. https://doi.org/10.1007/s12035-022-03111-y.

40. Yan, R., Zhao, X., Lei, J., and Zhou, Q. (2019). Structure of the human LAT1-4F2hc heteromeric amino acid transporter complex. Nature *568*, 127–130. https://doi.org/10.1038/s41586-019-1011-z.

41. Zhang, Y., Cheng, Q., Xue, Y., Yao, K., Syeda, M.Z., Xu, J., Wu, J., Wang, Z., Tang, L., and Mu, Q. (2023). LAT1 targeted brain delivery of temozolomide and sorafenib for effective glioma therapy. Nano Res. *16*, 9743–9751. https://doi.org/10.1007/s12274-023-5568-3.

42. Augustyn, E., Finke, K., Zur, A.A., Hansen, L., Heeren, N., Chien, H.C., Lin, L., Giacomini, K.M., Colas, C., Schlessinger, A., and Thomas, A.A. (2016). LAT-1 activity of meta-substituted phenylalanine and tyrosine analogs. Bioorg. Med. Chem. Lett. *26*, 2616–2621. https://doi.org/10.1016/j.bmcl.2016.04.023.

43. Li, L., Zhang, Y., and Wang, J. (2017). Effects of ligand distribution on receptor-diffusion-mediated cellular uptake of nanoparticles. R. Soc. Open Sci. *4*, 170063. https://doi.org/10.1098/rsos.170063.

44. Jhaveri, A., and Torchilin, V. (2016). Intracellular delivery of nanocarriers and targeting to subcellular organelles. Expet Opin. Drug Deliv. *13*, 49–70. https://doi.org/10.1517/17425247.2015.1086745.

45. Varkouhi, A.K., Scholte, M., Storm, G., and Haisma, H.J. (2011). Endosomal escape pathways for delivery of biologicals. J. Control Release *151*, 220–228. https://doi.org/10.1016/j.jconrel.2010.11.004.

46. Roberts, T.C., Langer, R., and Wood, M.J.A. (2020). Advances in oligonucleotide drug delivery. Nat. Rev. Drug Discov. *19*, 673–694. https://doi.org/10.1038/s41573-020-0075-7.

47. Anthony, K. (2022). RNA-based therapeutics for neurological diseases. RNA Biol. *19*, 176–190. https://doi.org/10.1080/15476286.2021.2021650.

48. Koh, H.S., Lee, S., Lee, H.J., Min, J.W., Iwatsubo, T., Teunissen, C.E., Cho, H.J., and Ryu, J.H. (2021). Targeting MicroRNA-485-3p Blocks Alzheimer's Disease Progression. Int. J. Mol. Sci. *22*, 13136. https://doi.org/10.3390/ijms222313136.

49. Ryu, I.S., Kim, D.H., Cho, H.J., and Ryu, J.H. (2023). The role of microRNA-485 in neurodegenerative diseases. Rev. Neurosci. *34*, 49–62. https://doi.org/10.1515/revneuro-2022-0039.

50. Behzadi, S., Serpooshan, V., Tao, W., Hamaly, M.A., Alkawareek, M.Y., Dreaden, E.C., Brown, D., Alkilany, A.M., Farokhzad, O.C., and Mahmoudi, M. (2017). Cellular uptake of nanoparticles: journey inside the cell. Chem. Soc. Rev. *46*, 4218–4244. https://doi.org/10.1039/c6cs00636a.

51. Satzer, P., Svec, F., Sekot, G., and Jungbauer, A. (2016). Protein adsorption onto nanoparticles induces conformational changes: Particle size dependency, kinetics, and mechanisms. Eng. Life Sci. *16*, 238–246. https://doi.org/10.1002/elsc.201500059.

52. Zhang, W., Taheri-Ledari, R., Ganjali, F., Mirmohammadi, S.S., Qazi, F.S., Saeidirad, M., KashtiAray, A., Zarei-Shokat, S., Tian, Y., and Maleki, A. (2022). Effects of morphology and size of nanoscale drug carriers on cellular uptake and internalization process: a review. RSC Adv. *13*, 80–114. https://doi.org/10.1039/d2ra06888e.

53. Hersh, A.M., Alomari, S., and Tyler, B.M. (2022). Crossing the Blood-Brain Barrier: Advances in Nanoparticle Technology for Drug Delivery in Neuro-Oncology. Int. J. Mol. Sci. *23*, 4153. https://doi.org/10.3390/ijms23084153.

54. Sonavane, G., Tomoda, K., and Makino, K. (2008). Biodistribution of colloidal gold nanoparticles after intravenous administration: effect of particle size. Colloids Surf. B Biointerfaces *66*, 274–280. https://doi.org/10.1016/j.colsurfb.2008.07.004.

55. Choi, H.S., Liu, W., Misra, P., Tanaka, E., Zimmer, J.P., Itty Ipe, B., Bawendi, M.G., and Frangioni, J.V. (2007). Renal clearance of quantum dots. Nat. Biotechnol. *25*, 1165–1170. https://doi.org/10.1038/nbt1340.

56. Faria, M., Björnmalm, M., Thurecht, K.J., Kent, S.J., Parton, R.G., Kavallaris, M., Johnston, A.P.R., Gooding, J.J., Corrie, S.R., Boyd, B.J., et al. (2018). Minimum information reporting in bio-nano experimental literature. Nat. Nanotechnol. *13*, 777–785. https://doi.org/10.1038/s41565-018-0246-4.

57. Banerjee, S.S., Aher, N., Patil, R., and Khandare, J. (2012). Poly(ethylene glycol)-Prodrug Conjugates: Concept, Design, and Applications. J. Drug Deliv. *2012*, 103973. https://doi.org/10.1155/2012/103973.

58. Li, W., Li, M., and Qi, J. (2021). Nano-Drug Design Based on the Physiological Properties of Glutathione. Molecules *26*, 5567. https://doi.org/10.3390/molecules26185567.

59. Cheng, R., Feng, F., Meng, F., Deng, C., Feijen, J., and Zhong, Z. (2011). Glutathione-responsive nano-vehicles as a promising platform for targeted intracellular drug and gene delivery. J. Contr. Release *152*, 2–12. https://doi.org/10.1016/j.jconrel.2011.01.030.

60. Dringen, R., and Hirrlinger, J. (2003). Glutathione pathways in the brain. Biol. Chem. *384*, 505–516. https://doi.org/10.1515/BC.2003.059.

61. Sun, X., Shih, A.Y., Johannssen, H.C., Erb, H., Li, P., and Murphy, T.H. (2006). Two-photon imaging of glutathione levels in intact brain indicates enhanced redox buffering in developing neurons and cells at the cerebrospinal fluid and blood-brain interface. J. Biol. Chem. *281*, 17420–17431. https://doi.org/10.1074/jbc.M601567200.

62. Such, G.K., Yan, Y., Johnston, A.P.R., Gunawan, S.T., and Caruso, F. (2015). Interfacing materials science and biology for drug carrier design. Adv. Mater. *27*, 2278–2297. https://doi.org/10.1002/adma.201405084.

63. Smith, S.A., Selby, L.I., Johnston, A.P.R., and Such, G.K. (2019). The Endosomal Escape of Nanoparticles: Toward More Efficient Cellular Delivery. Bioconjugate Chem. *30*, 263–272. https://doi.org/10.1021/acs.bioconjchem.8b00732.

64. Mitchell, M.J., Billingsley, M.M., Haley, R.M., Wechsler, M.E., Peppas, N.A., and Langer, R. (2021). Engineering precision nanoparticles for drug delivery. Nat. Rev. Drug Discov. *20*, 101–124. https://doi.org/10.1038/s41573-020-0090-8.

65. Anraku, Y., Kuwahara, H., Fukusato, Y., Mizoguchi, A., Ishii, T., Nitta, K., Matsumoto, Y., Toh, K., Miyata, K., Uchida, S., et al. (2017). Glycaemic control boosts glucosylated nanocarrier crossing the BBB into the brain. Nat. Commun. *8*, 1001. https://doi.org/10.1038/s41467-017-00952-3.

66. Wang, J., Tian, S., Petros, R.A., Napier, M.E., and Desimone, J.M. (2010). The complex role of multivalency in nanoparticles targeting the transferrin receptor for cancer therapies. J. Am. Chem. Soc. *132*, 11306–11313. https://doi.org/10.1021/ja1043177.

67. Alkilany, A.M., Zhu, L., Weller, H., Mews, A., Parak, W.J., Barz, M., and Feliu, N. (2019). Ligand density on nanoparticles: A parameter with critical impact on nanomedicine. Adv. Drug Deliv. Rev. *143*, 22–36. https://doi.org/10.1016/j.addr.2019.05.010.

68. Tosi, G., Vandelli, M.A., Forni, F., and Ruozi, B. (2015). Nanomedicine and neurodegenerative disorders: so close yet so far. Expet Opin. Drug Deliv. *12*, 1041–1044. https://doi.org/10.1517/17425247.2015.1041374.

69. Takakusa, H., Iwazaki, N., Nishikawa, M., Yoshida, T., Obika, S., and Inoue, T. (2023). Drug Metabolism and Pharmacokinetics of Antisense Oligonucleotide Therapeutics: Typical Profiles, Evaluation Approaches, and Points to Consider Compared with Small Molecule Drugs. Nucleic Acid Therapeut. *33*, 83–94. https://doi.org/10.1089/nat.2022.0054.

70. Vellonen, K.S., Ihalainen, J., Boucau, M.C., Gosselet, F., Picardat, T., Gynther, M., Kanninen, K.M., White, A.R., Malm, T., Koistinaho, J., et al. (2017). Disease-Induced Alterations in Brain Drug Transporters in Animal Models of Alzheimer's Disease : Theme: Drug Discovery, Development and Delivery in Alzheimer's Disease Guest Editor: Davide Brambilla. Pharm. Res. (N.Y.) *34*, 2652–2662. https://doi.org/10.1007/s11095-017-2263-7.

71. Gynther, M., Puris, E., Peltokangas, S., Auriola, S., Kanninen, K.M., Koistinaho, J., Huttunen, K.M., Ruponen, M., and Vellonen, K.S. (2018). Alzheimer's Disease Phenotype or Inflammatory Insult Does Not Alter Function of L-Type Amino Acid Transporter 1 in Mouse Blood-Brain Barrier and Primary Astrocytes. Pharm. Res. (N.Y.) *36*, 17. https://doi.org/10.1007/s11095-018-2546-7.

72. Li, J., Liu, J., Li, S., Hao, Y., Chen, L., and Zhang, X. (2016). Antibody h-R3-dendrimer mediated siRNA has excellent endosomal escape and tumor targeted delivery ability, and represents efficient siPLK1 silencing and inhibition of cell proliferation, migration and invasion. Oncotarget *7*, 13782–13796. https://doi.org/10.18632/oncotarget.7368.

73. Ryu, I.S., Kim, D.H., Ro, J.Y., Park, B.G., Kim, S.H., Im, J.Y., Lee, J.Y., Yoon, S.J., Kang, H., Iwatsubo, T., et al. (2023). The microRNA-485-3p concentration in salivary exosome-enriched extracellular vesicles is related to amyloid beta deposition in the brain of patients with Alzheimer's disease. Clin. Biochem. *118*, 110603. https://doi.org/10.1016/j.clinbiochem.2023.110603.